

spread use are not yet available, it is clear that technologies are becoming more effective and reproducible. (see Freire and Wheeler [16] for a review). Of paramount importance in future work will be functional characterization of the devices when in contact with complex proteomic samples, evaluating, among other things, undesirable non-specific adhesion, long term operation, and the capacity to deliver the analytes of interest to the MS for analysis. In particular, the latter requires an efficient release of sample from MALDI targets or ionization when sprayed from a liquid containing salts, impurities and large abundance proteins that may conceal the desired signal.

Cross References

- ▶ Proteomics in Microfluidic Devices
- ▶ Integrated Micro Devices for Biological Applications
- ▶ Mass Spectrometry
- ▶ Digital Microfluidics
- ▶ Lab-on-a-Chip (General Philosophy)
- ▶ Applications Based on Electrowetting

References

1. Loo JA, Berhane B, Kaddis CS, Wooding KM, Xie Y, Kaufman SL, Chernushevich IV (2005) Electrospray ionization mass spectrometry and ion mobility analysis of the 20S proteasome complex. *J Am Soc Mass Spectrom* 16:998–1008
2. Eng JK, McCormack AL, Yates JR (1994) An Approach to Correlate Tandem Mass-Spectral Data of Peptides with Amino-Acid-Sequences in a Protein Database. *J Am Soc Mass Spectrom* 5:976–989
3. Birendra N, Pramanik A, Ganguly K, Gross ML (eds) (2002) *Applied electrospray mass spectrometry*. Marcel Dekker, Inc., New York
4. Kebarle P, Peschke M (2000) On the mechanisms by which the charged droplets produced by electrospray lead to gas phase ions. *Anal Chim Acta* 406:11–35
5. Mann M, Hendrickson RC, Pandey A (2001) Analysis of proteins and proteomes by mass spectrometry. *Annu Rev Biochem* 70:437–473
6. Xue QF, Foret F, Dunayevskiy YM, Zavracky PM, McGruer NE, Karger BL (1997) Multichannel microchip electrospray mass spectrometry. *Anal Chem* 69:426–430
7. Lazar IM, Ramsey RS, Sundberg S, Ramsey JM (1999) Subattomole-sensitivity microchip nanoelectrospray source with time-of-flight mass spectrometry detection. *Anal Chem* 71:3627–3631
8. Schilling M, Nigge W, Rudzinski A, Neyer A, Hergenroder R (2004) A new on-chip ESI nozzle for coupling of MS with microfluidic devices. *Lab Chip* 4:220–224
9. Xie J, Miao Y, Shih J, Tai YC, Lee TD (2005) Microfluidic platform for liquid chromatography-tandem mass spectrometry analyses of complex peptide mixtures. *Anal Chem* 77:6947–6953
10. Kameoka J, Orth R, Ilic B, Czaplowski D, Wachs T, Craighead HC (2002) An Electrospray Ionization Source for Integration with Microfluidics. *Anal Chem* 74:5897–5901
11. Yin NF, Killeen K, Brennen R, Sobek D, Werlich M, van de Goor TV (2005) Microfluidic chip for peptide analysis with an integrated HPLC column, sample enrichment column, and nano-electrospray tip. *Anal Chem* 77:527–533
12. Fortier MH, Bonnell E, Goodley P, Thibault P (2005) Integrated microfluidic device for mass spectrometry-based proteomics and its application to biomarker discovery programs. *Anal Chem* 77:1631–1640
13. Brivio M, Tas NR, Goedbloed MH, Gardeniers HJGE, Verboom W, Van Den Berg A, Reinhoudt DN (2005) A MALDI-chip integrated system with a monitoring window. *Lab Chip* 5:378–381
14. Musyimi HK, Guy J, Narcisse DA, Soper SA, Murray KK (2005) Direct coupling of polymer-based microchip electrophoresis to online MALDI-MS using a rotating ball inlet. *Electrophoresis* 26:4703–4710
15. Gustafsson M, Hirschberg D, Palmberg C, Jornvall H, Bergman T (2004) Integrated Sample Preparation and MALDI Mass Spectrometry on a Microfluidic Compact Disk. *Anal Chem* 76:345–350
16. Freire SLS, Wheeler AR (2006) Proteome-on-a-chip: Mirage, or on the horizon? *Lab Chip* 6:1415–1423
17. Gundry RL, Edward R, Kole TP, Sutton C, Cotter RJ (2005) Disposable hydrophobic surface on MALDI targets for enhancing MS and MS/MS data of peptides. *Anal Chem* 77:6609–6617
18. Little DP, Cornish TJ, O'Donnell MJ, Braun A, Cotter RJ, Köstet H (1997) MALDI on a Chip: Analysis of Arrays of Low-Femtomole to Subfemtomole Quantities of Synthetic Oligonucleotides and DNA Diagnostic Products Dispensed by a Piezoelectric Pipet. *Anal Chem* 69:4540–4546
19. Wang YX, Zhou Y, Balgley BM, Cooper JW, Lee CS, DeVoe DL (2005) Electrospray interfacing of polymer microfluids to MALDI-MS. *Electrophoresis* 26:3631–3640
20. Moon H, Wheeler AR, Garrell RL, Loo JA, Kim CJ (2006) An integrated digital microfluidic chip for multiplexed proteomic sample preparation and analysis by MALDI-MS. *Lab Chip* 6:1213–1219

Interface Tracking

- ▶ Interface Capturing Schemes for Free-Surface Flows

Interfacial Electrohydrodynamics

- ▶ Interfacial Electrokinetic Flow

Interfacial Electrokinetic Flow

LESLIE YEO
 Micro/Nanophysics Research Laboratory
 Department of Mechanical Engineering, Monash
 University, Clayton Campus, Clayton, VIC, Australia
 leslie.yeo@eng.monash.edu.au

Synonyms

Free surface electrokinetics; Interfacial electrohydrodynamics; Free surface electrohydrodynamics

Definition

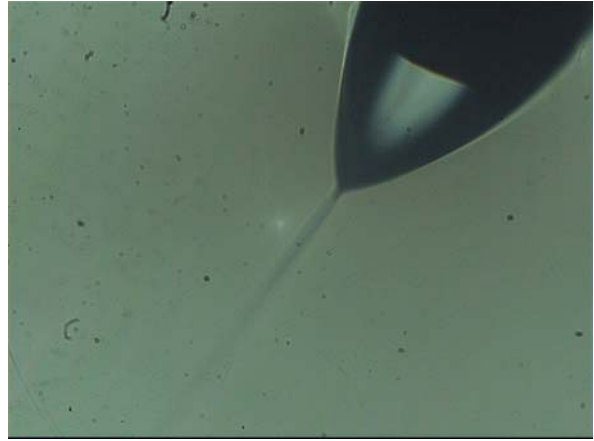
The term interfacial electrokinetic flow here encompasses all electrokinetically driven flows involving free-surfaces or freely deforming boundaries, i. e., gas–liquid interfaces or immiscible liquid–liquid interfaces.

Overview

Free surfaces are commonly encountered in many microfluidic applications. One class of free surface microfluidic applications involves individual or discrete drops and sprays, the former being termed *digital microfluidics*. Another class of free surface microfluidic applications is that which involves two-phase microchannel flows wherein either a gas bubble or stream flows within or adjacent to a liquid stream, or, a liquid phase flows within an immiscible liquid continuum (i. e., a *microemulsion*), or, a liquid stream stratifies another immiscible liquid stream. These classifications are, however, not mutually exclusive. For example, discrete drops or sprays are not just limited to open microfluidic systems, where they are exposed to an ambient environment. Often, to prevent evaporation, for example, the discrete drops are housed within an oil layer. Alternatively, a liquid spray can be encased within an immiscible liquid medium as a means for generating microemulsions.

In addition to the usual mathematical difficulties associated with free surface problems, the consideration of free surfaces becomes extremely important in microfluidics, especially given the increasing dominance of surface forces over body forces as the surface area to volume ratio increases with miniaturization. In addition, the curvature of the free surface becomes commensurate with the characteristic length scale of the system at these small scales. For example, the bubbles generated due to electrode reactions in electrokinetic microdevices can have dimensions which are on the same order as the microchannel width or height.

Electrokinetics is currently the preferred method for moving and transporting fluids in microchannels due to the ease of electrode fabrication and since electrokinetic mechanisms involve no moving mechanical parts which are prone to reliability concerns. Whilst significant progress has been achieved in understanding electrokinetic phenomena in the context of microfluidic technology, there is still a significant need to increase our fundamental understanding concerning the underlying complex hydrodynamic and physicochemical behavior associated with



Interfacial Electrokinetic Flow, Figure 1 Liquid meniscus issuing from a 100 μm capillary in DC electro spraying showing its conical shape and a thin jet that emanates from the meniscus tip. The jet subsequently breaks up due to hydrodynamic or Coulombic instabilities to generate very small aerosol drops

interfacial electrokinetic systems such as electro spraying or electrohydrodynamic atomization, electrospinning, electrocapillarity, electrowetting, electrokinetically-driven bubble transport and electrohydrodynamically-induced surface and bulk recirculation.

Basic Methodology

Governing Equations

For a Newtonian, incompressible fluid, the governing hydrodynamic equations are stipulated by the conservation of mass and momentum:

$$\nabla \cdot \mathbf{u} = 0, \quad (1)$$

$$\rho (\mathbf{u}_t + \mathbf{u} \cdot \nabla \mathbf{u}) = \nabla \cdot \mathbf{T}, \quad (2)$$

where \mathbf{u} is the velocity vector, ρ the fluid density and the subscript t denotes a time derivative. In Eq. (2),

$$\mathbf{T} = -p\mathbf{I} + \mu \left[\mathbf{n} \cdot \left(\nabla \mathbf{u} + \nabla \mathbf{u}^T \right) \cdot \mathbf{t} \right] + \mathbf{T}_M, \quad (3)$$

is the total stress tensor, comprising of the hydrostatic stress component, in which p is the fluid pressure and \mathbf{I} the identity tensor, the viscous stress component, in which μ is the fluid viscosity, and, \mathbf{n} and \mathbf{t} the unit outward normal and tangential vectors, respectively, and, a electric (Maxwell) stress component \mathbf{T}_M . In the above, the superscript T denotes the transpose of the tensor $\nabla \mathbf{u}$.

The coupling between the hydrodynamics and the electric field therefore arises through the Maxwell stress tensor. The total electric force density comprises the sum of the

Coulombic force arising from the presence of free charges and the dipole force arising due to the existence of bound charges:

$$\mathbf{f} = \rho_e \mathbf{E} + \mathbf{P} \cdot \nabla \mathbf{E}, \quad (4)$$

where ρ_e is the free space charge density, $\mathbf{E} = -\nabla\phi$ the electric field vector and \mathbf{P} the polarizability vector; ϕ is the electric potential. It can then be shown that for an electrically linear and isotropic medium, Eq. (4) can be expressed as [1]

$$\mathbf{f} = \rho_e \mathbf{E} - \frac{\varepsilon_0}{2} \nabla \left(\varepsilon - \rho \left. \frac{\partial \varepsilon}{\partial \rho} \right|_T \right) \mathbf{E} \cdot \mathbf{E}, \quad (5)$$

in which ε is the dielectric constant and ε_0 is the permittivity of free space. The second term in the parenthesis comprises a ponderomotive force term arising due to the inhomogeneity of the dielectric permeability, represented by a jump in ε , and an electrostrictive term at constant temperature T which accounts for the compressibility of the media. For incompressible fluids, electrostriction effects are negligible and hence this term can be omitted. Equation (5) can be expressed in terms of a divergence of a tensor $\mathbf{f} = \nabla \cdot \mathbf{T}_M$, from which we obtain an expression for the Maxwell stress tensor:

$$\mathbf{T}_M = \varepsilon \varepsilon_0 \mathbf{E} \mathbf{E} - \frac{\varepsilon \varepsilon_0}{2} (\mathbf{E} \cdot \mathbf{E}) \mathbf{I}. \quad (6)$$

The net Maxwell stress at an interface then has the following normal and tangential components:

$$\begin{aligned} \mathbf{T}_{M_n} &= \mathbf{n} \cdot \mathbf{T}_M \cdot \mathbf{n} \quad (7) \\ &= \frac{1}{2} \left[\varepsilon (\mathbf{E} \cdot \mathbf{n})^2 - \varepsilon (\mathbf{E} \cdot \mathbf{t}_1)^2 - \varepsilon (\mathbf{E} \cdot \mathbf{t}_2)^2 \right]_i^o, \\ \mathbf{T}_{M_t} &= \mathbf{n} \cdot \mathbf{T}_M \cdot \mathbf{t}_i = \varepsilon [\mathbf{E} \cdot \mathbf{n}]_i^o (\mathbf{E} \cdot \mathbf{t}_i), \quad (8) \end{aligned}$$

respectively, where \mathbf{t}_1 and \mathbf{t}_2 are the unit vectors orthogonally tangent to the interface. The square parenthesis $[\]_i^o$ denotes a jump in the inner quantity across the interface, obtained by subtracting the quantity of the inner phase i from that of the outer phase o .

In both phases, the electrostatic behavior can be described by Gauss' law:

$$\nabla \cdot \mathbf{E} = \nabla \cdot (-\nabla\varphi) = -\nabla^2\varphi = \frac{\rho_e}{\varepsilon \varepsilon_0}. \quad (9)$$

In addition, the condition of electric field irrotationality also holds:

$$\nabla \times \mathbf{E} = 0. \quad (10)$$

Charge conservation also requires

$$\nabla \cdot \mathbf{i} = \frac{\partial \rho_e}{\partial t}. \quad (11)$$

in which

$$\mathbf{i} = -\sigma \mathbf{E} - D \nabla \rho_e + \rho_e \mathbf{u}, \quad (12)$$

is the current density. In Eq. (12), σ is the electrical conductivity and D is the ion diffusivity.

Boundary Conditions

A free surface or a deformable interface between two fluid phases requires that fluid particles move only tangentially along the interface. As such, if the position of the interface Γ in a Cartesian coordinate system (x, y, z) is geometrically defined by $z = h(x, y, t)$, then, given that the interface itself is a streamline, a Lagrangian description of a fluid particle as it follows the streamline can be geometrically described by the implicit function

$$F(x, y, z, t) = z - h(x, y, t) = 0. \quad (13)$$

In the Eulerian reference frame, the material derivative of F , i. e., $DF/Dt = (\partial F/\partial t) + \mathbf{u} \cdot \nabla F$ must be equal to zero, which then leads to the kinematic boundary condition [2]:

$$\frac{\partial h}{\partial t} + u_n \mathbf{n} \cdot \nabla h = 0, \quad (14)$$

where u_n is the normal velocity and $\mathbf{n} = \nabla h / |\nabla h|$ is the outward unit vector normal to the interface.

The hydrodynamic boundary condition at the interface Γ is given by

$$\mathbf{n} \cdot [\mathbf{u}]_i^o = 0. \quad (15)$$

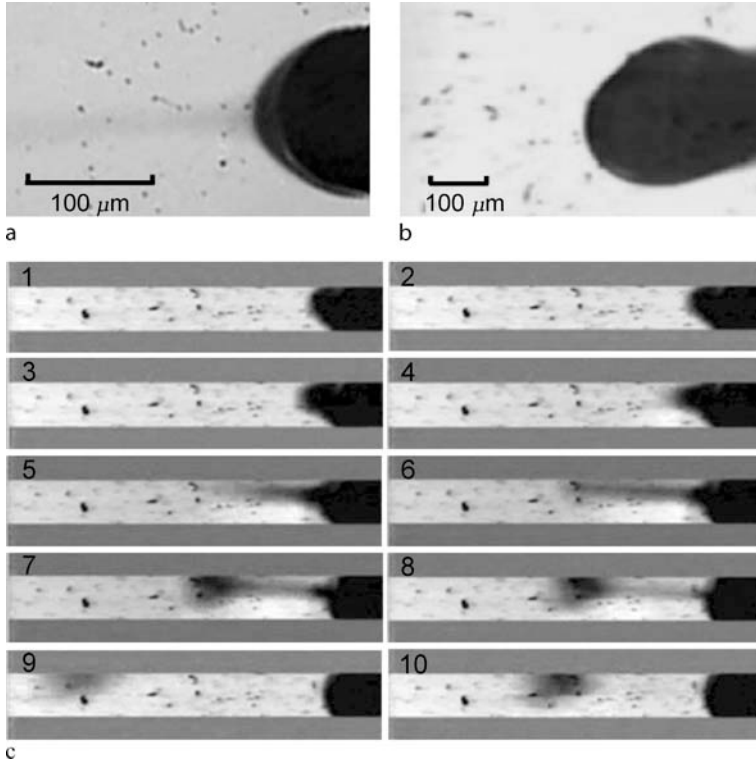
In addition, we also require continuity of shear stresses and the jump in the normal stress across the interface at Γ :

$$[\mathbf{n} \cdot \mathbf{T} \cdot \mathbf{t}]_i^o = 0, \quad (16)$$

and

$$[\mathbf{n} \cdot \mathbf{T} \cdot \mathbf{n}]_i^o = \gamma \kappa, \quad (17)$$

where γ is the interfacial tension and $\kappa = \nabla_s \cdot \mathbf{n}$ is twice the mean curvature of the interface in which $\nabla_s \equiv \nabla \cdot (\mathbf{I} - \mathbf{nn})$ is the surface gradient operator.



Interfacial Electrokinetic Flow, Figure 2 AC electro spray modes [11, 12]. (a) Tip streaming mechanism by which aerosol drops are periodically ejected from a resonating meniscus due to viscous-capillary forces. (b) Electrowetting phenomenon at high voltages which causes liquid to recede up the capillary thus suppressing drop ejection. (c) Sequence of images at 6000 fps showing the formation of a long slender microjet due to viscous-inertia forcing from which a drop is ejected

The remaining boundary conditions are given by the continuity of electric potential and electric stresses at the interface at Γ :

$$[\varphi]_i^o = 0, \quad (18)$$

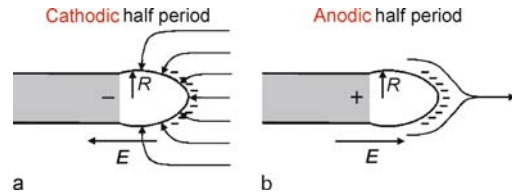
$$[\mathbf{E} \cdot \mathbf{t}]_i^o = 0, \quad (19)$$

$$[\varepsilon \mathbf{E} \cdot \mathbf{n}]_i^o = q, \quad (20)$$

in which q is the surface charge density at the interface Γ , which from Eq. (11), obeys

$$q_t + \mathbf{u} \cdot \nabla_s q = q \mathbf{n} \cdot (\mathbf{n} \cdot \nabla) \mathbf{u} - [\sigma \mathbf{E}]_i^o \cdot \mathbf{n}. \quad (21)$$

In the above, the subscripts i and o refer to the inner and outer phases respectively. The terms on the right of Eq. (21) represent the changes in the interfacial charge density due to surface dilation and electromigration, respectively. Also, the diffusion term has been neglected in Eq. (21), which is justifiable for sufficiently high field strengths typical in electrokinetic applications where the dimensionless field intensity $eV/k_B T \gg 1$, in which e is

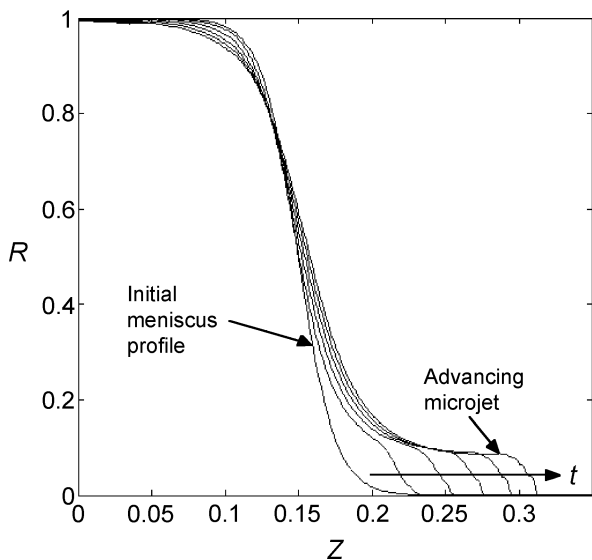


Interfacial Electrokinetic Flow, Figure 3 Plasma polarization mechanism in AC electro spraying [11]. (a) In the cathodic half period of the AC forcing cycle, the negative plasma generated forms a thin conducting layer surrounding the meniscus. As a result, the external electric field coincides with the interface in a normal orientation. (b) In the anodic half period, no plasma is generated. However, because there is insufficient time for the plasma to disperse due to diffusion, the plasma layer remains, thereby screening the external electric field. Consequently, the electric field is predominantly tangential to the interface

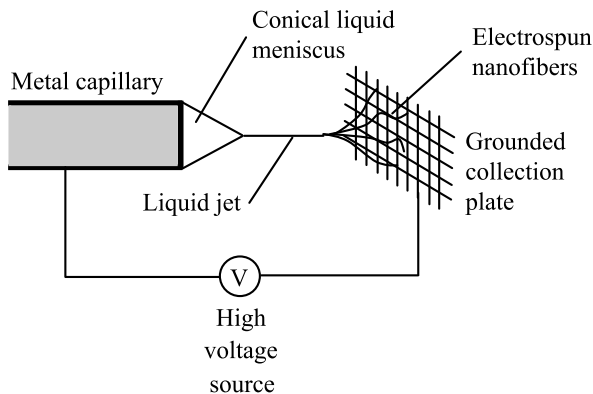
the electron charge, V the applied potential, k_B the Boltzmann constant and T the absolute temperature [3].

Key Research Findings

In this section, we discuss recent developments on various interfacial electrokinetic flow phenomenon that have

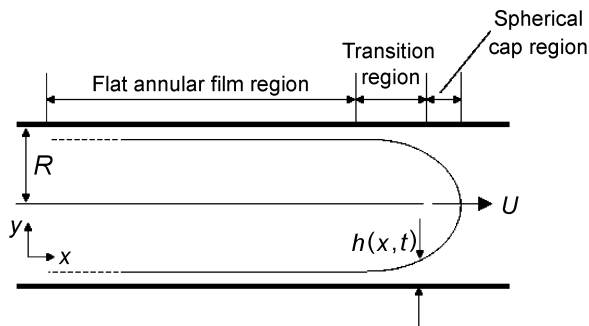


Interfacial Electrokinetic Flow, Figure 4 Spatio-temporal evolution profiles of the electro spray meniscus height R showing the initial stages of microjet formation obtained through an axisymmetric longwave model [11]

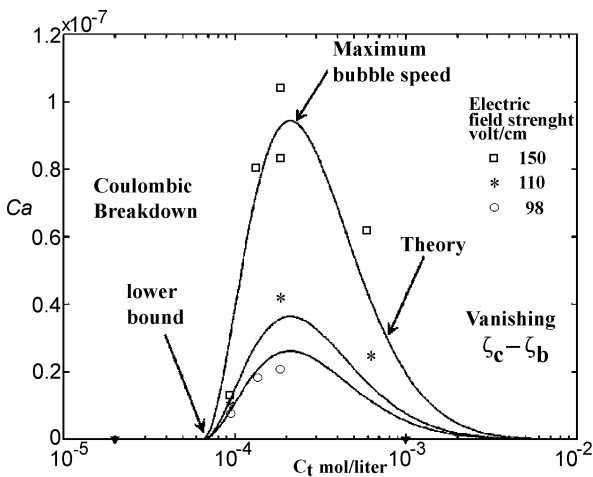


Interfacial Electrokinetic Flow, Figure 5 Schematic illustration of the electrospinning setup for the generation of nanometer and micron sized fibers

potential applications in microfluidic devices. In particular, we focus on electrohydrodynamic atomization (or more commonly known as electro spraying) and electro spinning, electrokinetic bubble transport, and, electrohydrodynamically driven surface and bulk microflows. Electrocapillarity and electrowetting which are other examples of interfacial electrokinetic flows will not be discussed here; the reader is referred to the more detailed entries on electrocapillarity and electrowetting, as well as that on electrowetting applications. The reader should also consult the reviews on electrowetting by Mugele and Baret [4] and Yeo and Chang [5].



Interfacial Electrokinetic Flow, Figure 6 Schematic illustration of the front cap of a bubble translating in a long capillary tube. After Chang [16]

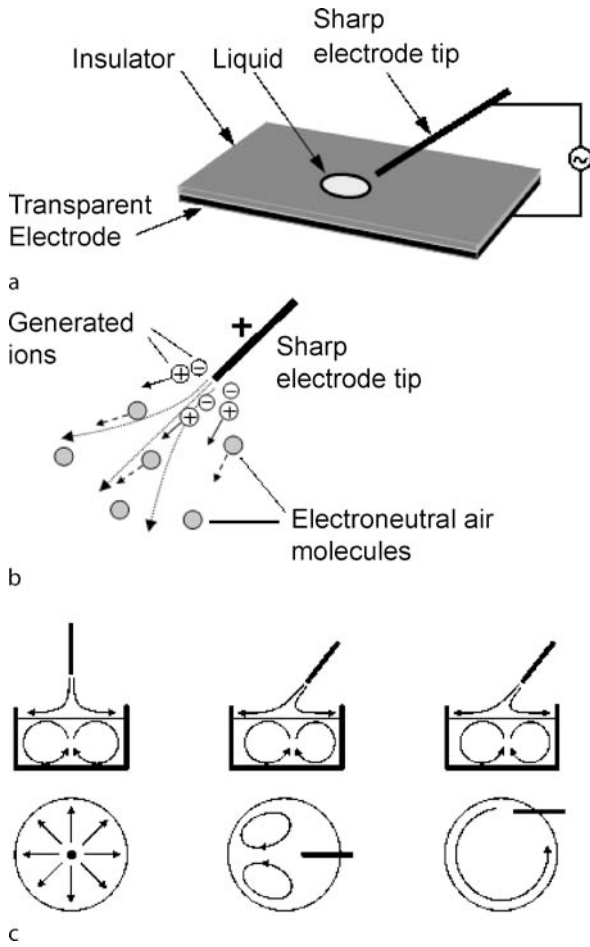


Interfacial Electrokinetic Flow, Figure 7 Electrokinetic bubble transport in a capillary. Dimensionless bubble speed represented by the capillary number Ca as a function of the total concentration of ionic surfactant C_t [17]

Electrospraying/Electrohydrodynamic Atomization

Electrospraying or electrohydrodynamic atomization is a mechanism for the generation of micron or nanometer dimension aerosols with the use of an applied electric stress [3]. DC electro spraying has been the subject of intense investigation over the past decade, in particular, due to its use as a soft ionization technique for the characterization of large complex and non-volatile biomolecules such as proteins and DNA in mass spectrometry. This technique is now known widely as electro spray ionization mass spectrometry or ESI-MS [6]. A balance between the Maxwell stress in Eq. (6) and the capillary stress gives an estimate of the critical voltage V_c required for electro spraying:

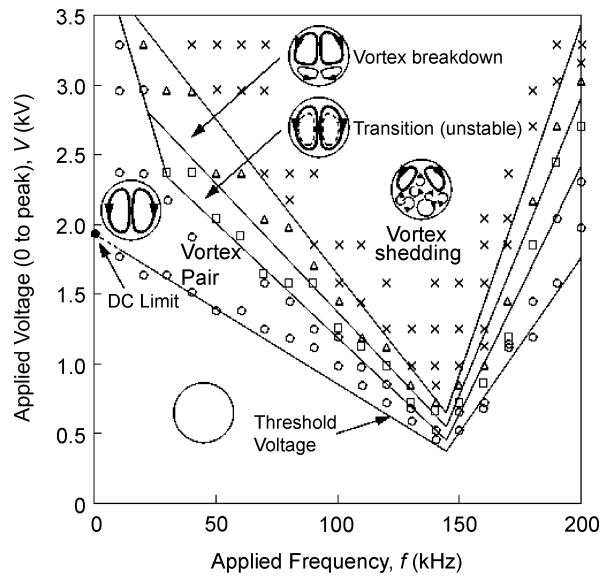
$$V_c \sim \sqrt{\frac{\gamma d^2}{\epsilon \epsilon_0 R}}, \tag{22}$$



Interfacial Electrokinetic Flow, Figure 8 Electrohydrodynamically induced surface recirculation. (a) Schematic depiction of the experimental setup. (b) Schematic illustration of the corona wind mechanism by which bulk electrohydrodynamic air thrust is generated. (c) Liquid recirculation patterns are generated depending on the orientation of the sharp electrode tip. After Yeo et al. [18, 19]

where d is the separation between nozzle and the ground electrode, and, R is the radius of curvature of the meniscus. Typically, $\gamma \sim 10^{-2} \text{ kg/s}^2$, $d \sim 10^{-2} \text{ m}$, $\epsilon\epsilon_0 \sim 10^{-10} \text{ C}^2/\text{Jm}$ and $R \sim 10^{-4} \text{ m}$, thus suggesting that extremely large voltages of order 10 kV are required for the onset of electrospaying.

In DC electrospaying, the absence of any external periodic forcing permits sufficient time for charge separation to occur within the liquid meniscus emanating from the nozzle orifice. Tangential ion conduction along a thin electric double layer at the meniscus interface is then responsible for co-ion accumulation, the repulsion of which then results in Coulombic fission wherein a thin liquid jet emanates from the tip once the Rayleigh limit is reached where the charge repulsion exceeds the surface force.

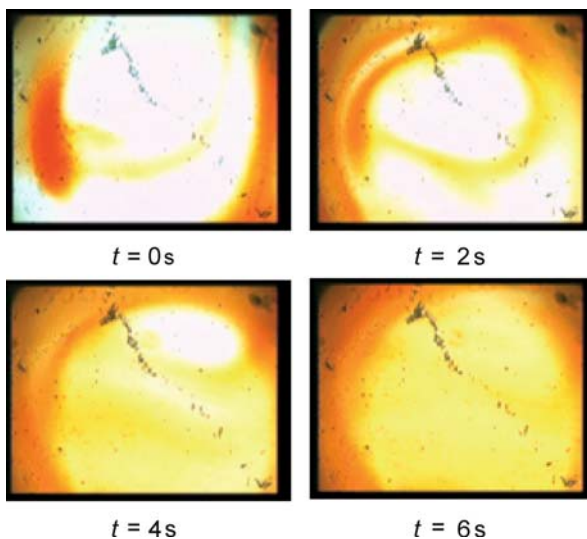


Interfacial Electrokinetic Flow, Figure 9 Liquid recirculation patterns as a function of the applied frequency and voltage. After Yeo et al. [18]

This charged jet then undergoes various hydrodynamic or Coulombic instabilities leading to its breakup and hence the generation of charged drops. These drops suffer from further disintegration when the drop evaporates leading to higher charge densities and hence the possibility of successive break up when the Rayleigh limit for Coulombic fission is exceeded. This disintegration cascade therefore gives rise to very small drops of nanometer order.

For perfectly conducting liquids, Taylor [7] showed that a conical meniscus with a half angle of 49.3° is produced by considering the static equilibrium balance between the capillary and Maxwell stresses in Eqs. (3), (6) and (17). In the perfect conducting limit, the drop is held at constant potential and hence the gas-phase electric field at the meniscus interface is predominantly in the normal direction. It can then be shown that the normal gas phase electric field $E_{n,g}$ scales as $1/R^{1/2}$ in which R is the meniscus radius which then stipulates from Eq. (7) that the Maxwell pressure $p_M \sim E_{n,g}^2$ scales as $1/R$, therefore exactly balancing the azimuthal capillary pressure $p_C \sim \gamma/R$ for all values of R . This exact balance, and absence of a length scale selection, is responsible for the formation of a static Taylor cone (Fig. 1) in the dominant cone-jet mode in DC electrospays [8].

Li et al. [9] and Stone et al. [10] later extended Taylor's perfectly conducting limit to allow for the effect of finite liquid conductivities, showing in these cases that the tangential electric field within the slender conical liquid meniscus dominates. However, the tangential liquid phase electric field $E_{t,l}$ also scales as $1/R$ and thus an exact bal-



Interfacial Electrokinetic Flow, Figure 10 Demonstration of rapid micro-mixing via the electrohydrodynamically induced surface microvortices in a microfluidic chamber 8 mm in diameter and 4 mm in height. After Yeo et al. [18]

ance between the Maxwell stress $p_M \sim E_{t,1}^2$ and the capillary stress p_C is again obtained, giving rise to a cone-like structure [11]. The cone angle, however, depends critically on the liquid to gas permittivity ratio $\beta \equiv \epsilon_l/\epsilon_g$; the Taylor angle is then recovered in the perfectly conducting limit as $\beta \rightarrow \infty$.

High frequency ($10 \text{ kHz} \leq \omega \leq 200 \text{ kHz}$) AC electro-sprays [11–13], on the other hand, behave very differently from DC electro-sprays. The drops generated are larger (of order microns) than the nanometer dimension DC electro-spray drops. In addition, the Taylor cone characteristic of DC electro-sprays is not observed. Instead, the drops are ejected from a curved meniscus or from a peculiar microjet that protrudes intermittently from the meniscus, as shown in Fig. 2. The high frequency periodic forcing does not permit sufficient time for charge separation to occur and hence co-ions accumulate at the meniscus tip, thereby rendering the ejected drops electroneutral. This explains the absence of Coulombic fission and hence the observation of larger drops since the Coulombic fission disintegration cascade does not occur. The drop electroneutrality allows the AC electro-spray to be used for drug delivery applications in which charged aerosols that could possibly lead to surface adsorption and compound ionization are undesirable [13]. Moreover, the absence of drop charge also stipulates that the current and hence power requirement is negligible, allowing the technology to be miniaturized for portable consumer use [11–13].

The absence of tangential ion conduction also results in a weaker liquid phase tangential electric field. As such, the AC electro-spray behavior was found to be insensitive to liquid conductivity [12]. This passivity of the liquid phase is compounded by the formation of a thin, highly-conducting, permanent negatively charged plasma polarization layer that envelops the liquid meniscus, giving rise to a dominant normal gas phase electric field in one AC half period [11]. This negative charge does not originate within the drop due to the insufficient time for charge separation within the liquid phase. In addition, the drop ejection time, roughly 10^{-3} s , is much larger than the period associated with the AC forcing frequency thus allowing any charge within the drop to essentially equilibrate during the ejection event [12].

Given that the AC electro-spray requires a working liquid of sufficiently high volatility (e.g., alcohols), the negatively charged plasma cloud could possibly arise due to evaporation and subsequent ionization of the liquid from the meniscus when the applied voltage exceeds a threshold voltage associated with the ionization potential. In the cathodic half period, when the meniscus and capillary have the same polarity as the plasma cloud forming a thin highly conducting layer enveloping the meniscus, the local gas phase normal electric field at the interface is significantly enhanced, as illustrated in Fig. 3a, since the meniscus and the plasma layer both resemble constant potential bodies in which the interfacial field is predominantly normal. On the contrary, plasma is not generated in the anodic half period. Nevertheless, a plasma layer still surrounds the meniscus unless there is sufficient time for it to be dispersed. The plasma layer is now oppositely charged to the meniscus and capillary, effectively screening the external field such that a weak tangential gas phase field arises, as shown in Fig. 3b. However, the enhanced normal gas phase field in the cathodic half period dominates and hence, averaged over many cycles, produces a net Maxwell stress that is responsible for the meniscus dynamics observed [11].

This plasma polarization mechanism also explains the appearance of a minimum in the frequency dependent critical voltage of approximately 165 kHz for spraying to occur. Below this optimum frequency, as $\omega \rightarrow 0$, there is adequate time for the dispersion of the plasma generated away from the meniscus. Above this optimum frequency, as $\omega \rightarrow \infty$, there is insufficient time for the dispersion to occur. Maximum interfacial plasma polarization therefore occurs at the optimum frequency, therefore producing the largest enhancement of the local normal Maxwell field at the meniscus interface [11].

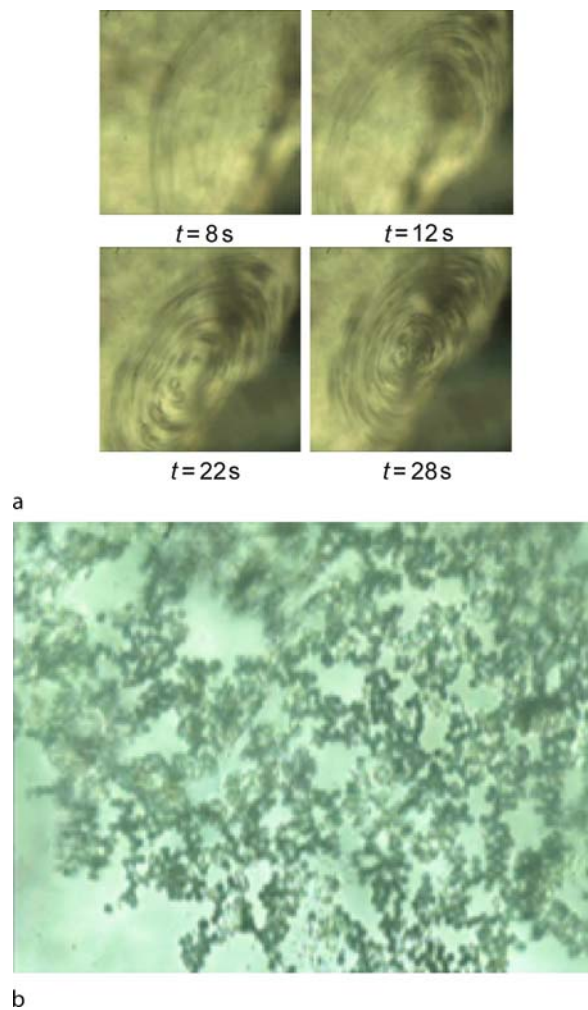
Since both meniscus and plasma layer resemble constant potential bodies, the solution of the Eq. (9) governing the gas phase electrostatics in the weak polarization limit

where ρ_e is negligible gives rise to a specific scaling for the normal interfacial gas phase electric field $E_{n,g}$. Assuming an arbitrary axisymmetric meniscus shape but not precluding the existence of a conical geometry, it can be shown from spheroidal harmonics that $E_{n,g} \sim 1/R^{1/2}$ for a sharp conical meniscus. On the other hand, $E_{n,g} \sim 1/R$ is obtained for more slender bodies such as an elongated ellipsoid or cylinder. Nevertheless, given that the more singular $1/R$ scaling for a slender geometry dominates at the meniscus tip, as $R \rightarrow 0$, the Maxwell pressure $p_M \sim E_{n,g}^2$ scales as $1/R^2$ and hence an exact balance with the azimuthal capillary pressure $p_C \sim \gamma/R$ is only possible for one specific value of R [11]. This length scale selection therefore excludes the possibility of a cone-like meniscus and instead suggests that the meniscus is stretched to a more elongated cylinder-like geometry such as that of the microjet shown in Fig. 2, thus suggesting why a non-steady microjet is produced in AC electrospays instead of a steady Taylor cone [11].

The role of the Maxwell pressure resulting from a normal gas phase interfacial electric field that scales as $1/R$ in elongating the liquid meniscus into a cylindrical microjet structure can also be verified through a dynamic simulation in which the equations governing the coupled interactions between the hydrodynamics (Eqs. (1)–(3)) and electrostatics (Eq. (9)) are solved simultaneously for a constant potential liquid meniscus in the longwave limit in axisymmetric polar coordinates $(r, 0, z)$, subject to the boundary conditions given by Eqs. (14)–(20). The polarization in the bulk gas phase is assumed to be weak, i. e., $\rho_e \sim 0$, such that Eq. (9) reduces to the Laplace equation. Further details of the model are given in [11]. A typical spatio-temporal evolution profile is illustrated in Fig. 4 in which an axial pressure gradient resulting from the interfacial distribution of the normal Maxwell stress with a $1/R^2$ scaling along the meniscus is observed to stretch the initially curved meniscus and pull out a slender microjet resembling that in Fig. 2. After a short transient, the microjet is observed to propagate forward at roughly constant velocity whilst maintaining an approximately constant radius [11].

Electrospinning

The electrospinning of micron and nanometer dimension fibers is a hybrid technology that arose out of electrospaying. In the past decade, fiber electrospinning has observed exponential growth in interest. However, the concept and technique has not evolved much from the original setup, shown in Fig. 5, which is very similar to that for electrospaying. A wide variety of polymer and polymer composite fibers with different morphologies (e. g., beaded,



Interfacial Electrokinetic Flow, Figure 11 (a) Demonstration of microparticle ($10\ \mu\text{m}$ latex particles) trapping and concentration within the electrohydrodynamically induced surface microvortices. (b) The particle aggregate remains intact as a planar interfacial colloidal crystal structure even after cessation of the flow upon removal of the applied electric field. After Yeo et al. [18]

pored, hollow, core-shell, etc.) have since been electrospun, examples of which are summarized in [14]. The AC electrospay setup has also been modified to synthesize fibers of micron order thickness from biodegradable polymeric excipients [13], although it should be mentioned that the mechanism by which the fibers are generated, predominantly due to extensional stresses that lead to the stretching of the microjet in Fig. 2 and subsequent solvent evaporation and hence jet solidification into a fiber, differs from that in DC electrospinning where the mechanism is largely due to evaporative solidification of the solvent from the thin jet that emanates from the Taylor cone as a result of Coulombic fission.

Electrospinning has been modeled through an analysis of electrically forced axisymmetric liquid jets [15], in which the asymptotic limit requirement of either assuming the liquid as a perfect conductor or a perfect dielectric is relaxed such that the existence of interfacial charge can be accounted through Eq. (21). This is because whilst bulk conduction can be neglected in the small free space charge density ρ_e limit, interfacial charge and hence conduction is not usually negligible. The existence of such charge also gives rise to a finite tangential Maxwell stress given by Eq. (8) which can only be balanced by the viscous stress. A similar axisymmetric model to that described above, assuming the jet to be slender such that the longwave approximation holds ($R_0 \ll L$, in which R_0 is the initial meniscus height and L the characteristic length scale of the jet), is then derived. In this limit, the external electric field can be simplified such that a slender dielectric meniscus can essentially be described as an effective axial line distribution of free and interfacially bound charges λ . An electric field flux balance on Gaussian surfaces S_1 and S_2 around and encompassing the meniscus interface then leads to [15]

$$\oint_{S_1} \mathbf{E} \cdot \mathbf{n} dA = \left[\left(\pi R^2 E_{t,1} \right)_z + 2\pi R E_{n,1} \right] dz = 0, \quad (23)$$

and

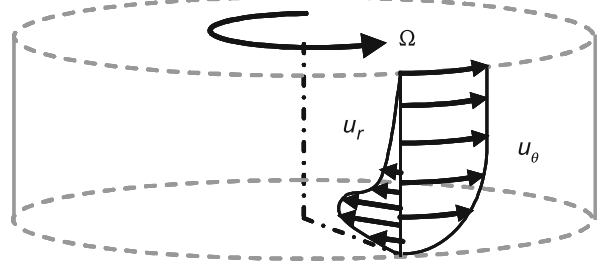
$$\oint_{S_2} \mathbf{E} \cdot \mathbf{n} dA = \left[\left(\pi R^2 E_{t,1} \right)_z + 2\pi R E_{n,g} \right] dz = 4\pi \lambda dz, \quad (24)$$

in which A denotes the area and the subscript z denotes derivatives in the axial direction. Equations (23) and (24) can be substituted into Coulomb's Law describing the gas phase electric potential in the region far from the interface [15]:

$$\Phi_g = \Phi_\infty + \int \frac{\lambda(z', t)}{\sqrt{r^2 + (z - z')^2}} dz', \quad (25)$$

where Φ_∞ is the applied potential, to yield a second order ordinary differential equation for the tangential electric field in the liquid phase [15]:

$$E_{t,1} - \ln \frac{R_0}{L} \left[\frac{1}{2} \left(\frac{\varepsilon_1}{\varepsilon_g} - 1 \right) \left(R^2 E_{t,1} \right)_{zz} - 4\pi (qR)_z \right] - E_\infty = 0, \quad (26)$$



Interfacial Electrokinetic Flow, Figure 12 Schematic depiction of the azimuthal and radial velocity profiles, u_θ and u_r , respectively, in Batchelor flows (liquid flow between rotating and stationary circular disks; the angular rotation is Ω). After Yeo et al. [19]

in which E_∞ denotes the applied electric field. The choice of boundary conditions at the nozzle orifice is also critical to the stability of the numerical solutions. A detailed discussion can be found in [15] and is also summarized in [14].

Electrokinetic Bubble Transport in Microchannels

Chang [16] showed that the pressure drop across a bubble translating in a microcapillary with speed U , as illustrated in Fig. 6, scales as $(\gamma/R)Ca^{2/3}$, which is essentially the difference in the capillary pressures between the cap pressures at the front and rear of the bubble; R is the capillary radius and $Ca \equiv \mu U/\gamma$ is the capillary number. Given that the pressure drop required to drive a liquid slug of length L at speed U is $\mu UL/R^2$, then the pressure drop across a bubble corresponds to an equivalent slug length of $RCa^{-1/3}$, obtained by balancing the pressure drop in both cases. Since Ca is typically between $10^{-8} - 10^{-4}$ in microcapillaries, this means that the pressure drop required to drive a bubble is extremely large to overcome the viscous dissipation associated with the bubble, and is equivalent to driving a liquid slug with a length that is several orders of magnitude of the capillary radius [16].

As the usual parabolic velocity profile of pressure-driven Poiseuille flow leads to the flowrate scaling as R^4 whereas the flat velocity profile obtained in pure electroosmotic flow gives rise to a flowrate that scales as R^2 , it can be seen that it is more efficient to drive microchannel flows where R becomes very small using electrokinetic flows as opposed to pressure-driven flow. However, there are some design issues to be considered in electrokinetic bubble transport.

From Ohm's law,

$$i = \frac{I}{AcL} = \sigma E, \quad (27)$$

where i is the current density, E the local electric field, I the corresponding current, and, A_c and L are the cross-sectional area and length of the capillary, respectively, we observe that $E \sim 1/A_c$. The electroosmotic slip velocity is given by

$$u_s = \frac{\varepsilon \varepsilon_0 \zeta E}{\mu}, \quad (28)$$

where ζ is the electrokinetic (or zeta-) potential, which stipulates that $u_s \sim 1/A_c$. It then follows from Eqs. (27) and (28) that the volumetric flowrate is

$$Q = u_s A_c = \frac{\varepsilon \varepsilon_0 \zeta I}{\mu \sigma L}, \quad (29)$$

which suggests that the flowrate due to electrokinetic flow is independent of the capillary cross-sectional area. This, and the fact that the electrokinetic flow velocity profile is virtually flat across the channel, is quite unfortunate because it requires the flow in the thin annular film around the bubble to be equal to the flow behind it. As a result, it is impossible to build up a back pressure driving force behind the bubble. The electrolyte simply flows around the bubble, rendering it stationary [16].

Thus, in order to drive bubble transport using electrokinetic flow, the flow invariance to the cross-section must be eliminated such that the flow in the annular film is less than the flow behind the bubble. Chang [16] proposes several ways to reduce the annular film flow by introducing drag at the bubble interface to retard the annular film (however, this only works if the bubble is essentially a viscous liquid drop) or by adding surfactants that reduce the local interfacial tension and hence generate Marangoni stresses (stresses arising due to interfacial tension gradients). Alternatively, it is also possible to introduce an ionic surfactant that resides at the bubble interface such that the double layer at the interface has an opposite charge to that of the capillary tube surface. Thus, the ζ -potential at the interface would have an opposite sign to that at the capillary surface. From the Smoluchowski slip in Eq. (28), we then note that the velocity at the bubble interface is in the opposite direction to that at the capillary surface. Careful control of the amount of ionic surfactants could also give rise to equal but opposite velocities, thus eliminating the flow in the annular film completely.

Figure 7 shows the dimensionless bubble translation speed Ca as a function of the surfactant (anionic surfactant since the glass capillary used has positive surface charge) ionic concentration for various electric field strengths [17]. At low concentrations, given that the Debye screening length scales as the inverse of the square root of the concentration, the electric double layer thickness becomes compa-

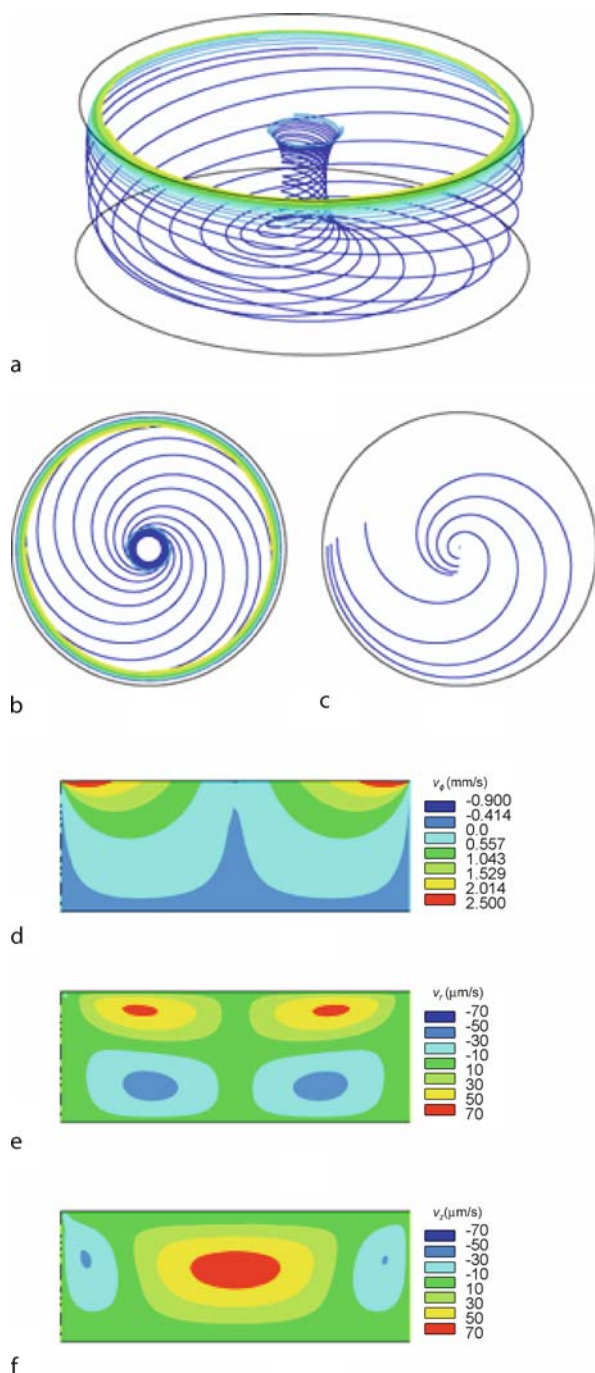
rable to the thickness of the annular film. The overlapping double layers of different polarities then leads to Coulombic attraction which causes the annular film to collapse. As such, there is a critical value for the ion concentration of approximately 10^{-5} mol/l before which bubble motion is observed. At high concentrations, however, the bubble speed again diminishes due to the vanishing electric double layer.

Electrohydrodynamically-Induced Interfacial Recirculation

Very recently, a novel way of driving liquid recirculation has been developed by exploiting a bulk electrohydrodynamic air thrust generated from a nearly singular electric field at a sharp electrode tip mounted a small height (~ 4 mm) above the liquid surface [18], as depicted in Fig. 8a. This air propulsion, also known as *corona wind* or *ionic wind*, arises when the voltage at the electrode tip exceeds the threshold ionization voltage leading to the breakdown of the air surrounding the electrode tip. Counter-ions are then repelled away from the electrode, colliding into the electroneutral air molecules along the way, as illustrated in Fig. 8b. The momentum transfer arising from these collisions then gives rise to the bulk air flow. By inclining the electrode such that the air flow is directed towards the liquid surface, interfacial shear then results in recirculation at the surface. Depending on the positioning of the needle, a clockwise or anti-clockwise motion or a pair of surface vortices can be generated (Fig. 8c). Figure 8c also shows the secondary bulk recirculation generated due to the primary surface flow; this will be discussed subsequently.

The voltage-frequency behavior is depicted in Fig. 9. We observe that the critical voltage to obtain liquid recirculation decreases with increasing applied frequency until approximately 145 kHz before increasing again. This optimum frequency is associated with the inverse RC time scale of the plasma charging mechanism [18], where R is the resistance and C the capacitance. At low frequencies as $\omega \rightarrow 0$, there is sufficient time for any plasma generated to diffuse away. At high frequencies as $\omega \rightarrow \infty$, on the other hand, there is insufficient time for plasma to be generated in each half AC period.

Moving diagonally across the voltage-frequency characteristic of Fig. 9 in the direction of increasing voltage and frequency also yields interesting behaviour in which the vortices become increasingly unstable, breaking down to spawn off additional vortex pairs. At yet higher voltages and frequencies, the vortex breakdown continues to produce a cascade of vortices with a continuum of length scales, similar to that observed in vortex shedding [18]. The stability of the original vortices can however be recovered by reducing the voltage at a fixed frequency.



Interfacial Electrokinetic Flow, Figure 13 Numerical flow simulation results of the secondary meridional flow arising from primary surface recirculation of the liquid. (a), (b) and (c) are flow field traces; (b) is a cross-sectional plan view of the flow field at the top surface and (c) is a cross-sectional plan view at a small distance just above the base. (d), (e) and (f) are circumferential θ , radial r and vertical z velocity profiles, respectively. Bright shades indicate motion along the respective axis directions and dark shades indicate motion against the axis direction. After Yeo et al. [19]

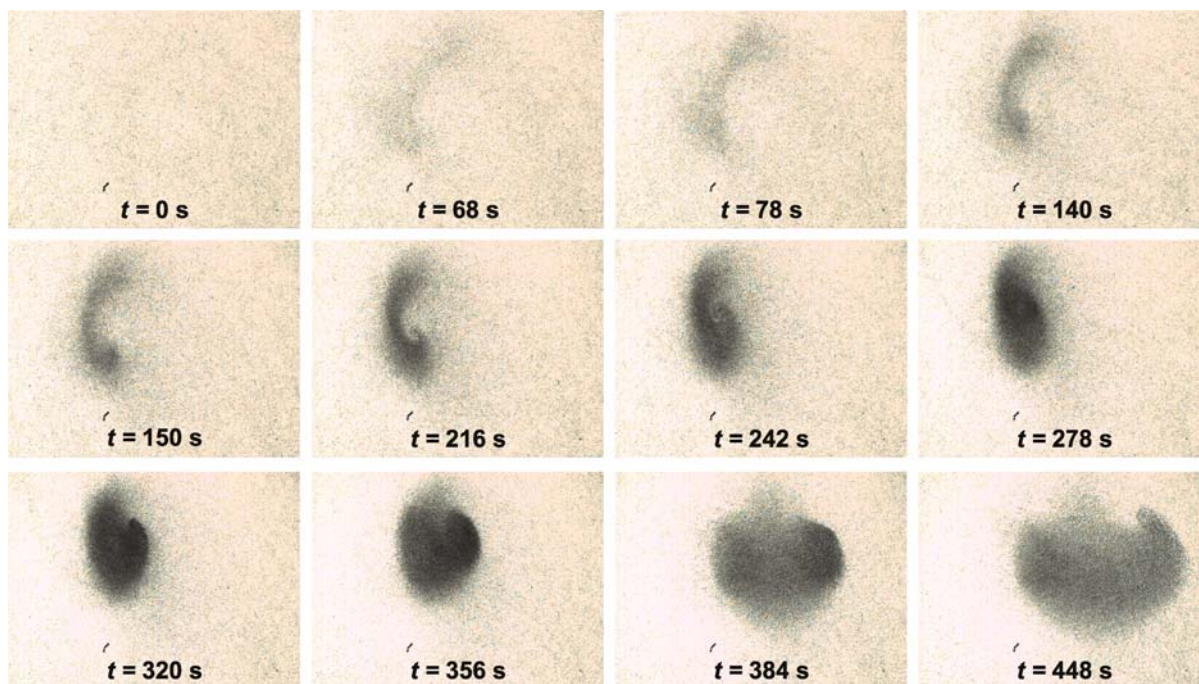
These surface vortices provide an efficient means for microfluidic mixing, as shown in Fig. 10 where a dye is rapidly mixed within several seconds. The mixing can be enhanced by inducing the vortex instabilities wherein turbulent-like mixing efficiencies are observed [18]. In addition, particles dispersed in the flow are also observed to be drawn into the vortices due to positive dielectrophoresis towards a point on the interface closest to the needle where the field is most intense. Once a sufficient particle concentration is achieved within the vortex, shear-induced migration leads to cross-streamline transport such that the interior of the vortex is populated [18], as shown in Fig. 11a. Upon relaxation of the electric field and hence termination of the flow, we observe the particle aggregate to remain intact, possibly due to van der Waals attraction (Fig. 11b). This therefore provides a mechanism for particle trapping and concentration.

The induced surface flow also gives rise to secondary bulk fluid motion, in the same way that bulk meridional vortices are generated in a fluid trapped between rotating and stationary disks in Batchelor flows [19], as depicted in Fig. 12. In this flow recirculation mode, particles dispersed in the flow are convected to the bottom by the bulk meridional recirculation. However, due to the inward radial velocity in the Ekman boundary layer (see Fig. 13), the particles begin to swirl in a helical-like manner towards the center of the base [19]. Although the flow recirculates back up a central spinal column, the gravitational force on the particle is sufficient to trap the particles at a pseudo-stagnation point at the base. This was demonstrated to be another mechanism for particle trapping and concentration. Figure 14 shows the efficient trapping of red blood cells for microfluidic blood plasma separation in several minutes [19].

These surface and bulk electrohydrodynamic recirculation, whilst having the usual advantages of electrokinetic devices wherein mechanically moving parts are absent, also benefit from low field penetration into the liquid given that the field is predominantly in the gas phase, thus posing little threat in lysing biological cells. In addition, the absence of electrode-sample contact also minimizes sample contamination through electrolytic reactions, non-specific adsorption of biological compounds or Joule heating [19].

Future Directions for Research

Electrokinetic flows in microchannels has been extensively studied over the past decade. However, there is still a need for a greater understanding of electrokinetic flows involving freely deforming surfaces such as electrospraying, electrospinning, electrowetting and electrohy-



Interfacial Electrokinetic Flow, Figure 14 Sequence of images showing the separation of red blood cells from blood plasma via the secondary meridional bulk liquid recirculation. The final plasma effluent above contains a hematocrit less than 0.003%. After Yeo et al. [19]

drodynamically induced surface flows. In particular, the complex physicochemical behavior at the interface and its coupling to the bulk flow is still not well understood. One example is how surface polarization and tangential ion conduction affects the flow behavior. There is also a further need for accurate theoretical models that are underpinned by a correct fundamental physical understanding of such systems. For example, free surface models developed for investigating the behavior of interfacial flows driven by Marangoni and thermocapillary stresses have been extended to study the effects of electrical stresses (see, for example, [20]). It is anticipated that these models will form the basis of other more complex free-surface electrohydrodynamic models to investigate interfacial flow behavior and stability.

Cross References

- ▶ [Applications Based on Electrowetting](#)
- ▶ [Bubble Dynamics in Microchannel](#)
- ▶ [Centrifugal Microfluidics](#)
- ▶ [Dielectrophoresis](#)
- ▶ [Digital Microfluidics](#)
- ▶ [Droplet and Bubble Formation in Microchannels](#)
- ▶ [Droplet Based Lab-on-a-Chip Devices](#)
- ▶ [Droplet Dispensing](#)
- ▶ [Droplet Dynamics in Microchannel](#)

- ▶ [Droplet Microreactors](#)
- ▶ [Electrocapillary](#)
- ▶ [Electrokinetic Two-Phase Flows](#)
- ▶ [Electrowetting](#)
- ▶ [Electrowetting and Droplets](#)
- ▶ [Interface Capturing Schemes for Free-Surface Flows](#)
- ▶ [Interface Tracking Schemes for Free-Surface Flows](#)
- ▶ [On-Chip Electro spray](#)
- ▶ [Surface Tension, Capillarity and Contact Angle](#)

References

1. Landau SC, Lifshitz EM (1960) *Electrodynamics of Continuous Media*. Pergamon, Oxford
2. Castellanos A, González A (1998) Nonlinear electrohydrodynamics of free surfaces. *IEEE Trans Dielect Elec Insul* 5:334–343
3. Saville DA (1997) *Electrohydrodynamics: The Taylor–Melcher leaky dielectric model*. *Ann Rev Fluid Mech* 29:27–64
4. Mugele F, Baret J-C (2005) *Electrowetting: From basics to applications*. *J Phys Cond Mat* 17:R705–R774
5. Yeo LY, Chang H-C (2005) Static and spontaneous electrowetting. *Mod Phys Lett B* 19:549–569
6. Fenn JB, Mann M, Meng CK, Wong SF, Whitehouse CM (1989) *Electrospray ionization for mass spectrometry of large biomolecules*. *Science* 246:64–71
7. Taylor G (1964) *Disintegration of water drops in an electric field*. *Proc Royal Soc London A* 280:383–397
8. Grace JM, Marijnissen JCM (1994) *A review of liquid atomization by electrical means*. *J Aero Sci* 25:1005–1019

9. Li H, Halsey TC, Lobkovsky A (1994) Singular shape of a fluid drop in an electric or magnetic field. *Europhys Lett* 27:575–580
10. Stone HA, Lister JR, Brenner MP (1999) Drops with conical ends in electric and magnetic fields. *Proc Royal Soc London A* 455:329–347
11. Yeo LY, Chang HC (2006) High frequency AC electrospays: Mechanisms and applications. In: Rahman M, Brebbia CA (eds) *Advances in Fluid Mechanics VI*. WIT, Southampton, pp 223–231
12. Yeo LY, Lastochkin D, Wang S-C, Chang H-C (2004) A new ac electrospay mechanism by Maxwell-Wagner polarization and capillary resonance. *Phys Rev Lett* 92:133902
13. Yeo LY, Gagnon Z, Chang H-C (2005) AC electrospay biomaterials synthesis. *Biomaterials* 26:6122–6128
14. Yeo LY, Friend JR (2006) Electrospinning carbon nanotube polymer composite nanofibers. *J Exp Nanosci* 1:177–209
15. Hohman MM, Shin M, Rutledge G, Brenner MP (2001) Electrospinning and electrically forced jets I. Stability theory, *Phys Fluid* 13:2201–2220
16. Chang H-C (2002) Bubble/Drop transport in microchannels. In: Gad-el-Hak M (ed) *The MEMS Handbook*. CRC, Boca Raton
17. Takhistov P, Indeikina A, Chang H-C (2002) Electrokinetic displacement of air bubbles in microchannels. *Phys Fluid* 14:1–14
18. Yeo LY, Hou D, Maheshwari S, Chang HC (2006) Electrohydrodynamic surface microvortices for mixing and particle trapping. *Appl Phys Lett* 88:233512
19. Yeo LY, Friend JR, Arifin DR (2006) Electric tempest in a teacup – The tea leaf analogy to microfluidic blood plasma separation. *Appl Phys Lett* 89:103516
20. Yeo LY, Chang HC (2006) Electrowetting films on parallel line electrodes. *Phys Rev E* 73:011605

Interfacial Flow

- ▶ [Interface Capturing Schemes for Free-Surface Flows](#)

Interfacial Flow Modelling

- ▶ [Numerical Techniques for Free Surface Flows: Interface Capturing and Interface Tracking](#)

Interfacial Instability

JEFFREY D. ZAHN
 Department of Biomedical Engineering, Rutgers, The State University of New Jersey, Piscataway, NJ, USA
 jdzahn@rci.rutgers.edu

Synonyms

Rayleigh instability; Bridging instability; Electrohydrodynamic instability; Rosensweig instability

Definition

Interfacial instabilities develop at an fluid–fluid or fluid–gas interface due to the unstable growth of interfacial perturbations. These instabilities may be surface tension driven (Rayleigh, liquid bridge instability), electrically driven (electrohydrodynamic instability) or magnetically driven (Rosensweig instability). These instabilities have been used in applications as diverse as inkjet printing to surface tension measurements. Interfacial instabilities are modeled using classical linear stability analysis considering momentum transport equations and both kinematic and interfacial stress boundary conditions. These models test the stability of the interfacial perturbations to infinitesimal disturbances.

Overview

The Rayleigh instability [1] is an example of a capillary driven instability which causes droplet breakup and has been used extensively for inkjet printing. Other interfacial instabilities such as a liquid bridge instability [2] have been studied to explore the stability criteria of coalescing two droplets from binary capillaries and determining whether the droplet will form a stable liquid bridge between the two capillary ends or if the bridge will rupture to have a droplet suspended on a single capillary end. Electrohydrodynamic instabilities occur when electrical stresses are applied at an interface. The electrical stresses develop at the interface primarily due to a conductivity or permittivity gradient between two fluid phases. The early work on modeling electrohydrodynamic instabilities performed a linear stability analysis of the electrical and fluid interfacial boundary conditions using the transfer relations developed by Melcher [3]. Melcher developed a dielectric model which describes liquids as being both polarizable and having free charge in an imposed electric field. Finally instabilities have been demonstrated using ferrofluids [4] which are colloidal suspensions of magnetic nanoparticles with a high magnetic susceptibility. When a ferrofluid is exposed to a magnetic field which is strong enough to promote instability, the surface of the fluid will spontaneously form a regular pattern of vertical spikes (peaking instability) consisting of the ferrofluid protruding from the initially flat interface.

Basic Methodology

The Rayleigh instability is the basis for most inkjet printing applications. When fluid is forced through an orifice (such as an inkjet printer head) a cylindrical fluid jet is produced with a fluid–air interface. As the jet falls under the influence of gravity it accelerates and is stretched so